

pubs.acs.org/cm Article

Dimensional Control over Metal Halide Perovskite Crystallization Guided by Active Learning

Zhi Li, Philip W. Nega, Mansoor Ani Najeeb Nellikkal, Chaochao Dun, Matthias Zeller, Jeffrey J. Urban, Wissam A. Saidi, Joshua Schrier, Alexander J. Norquist, and Emory M. Chan*



Cite This: https://doi.org/10.1021/acs.chemmater.1c03564



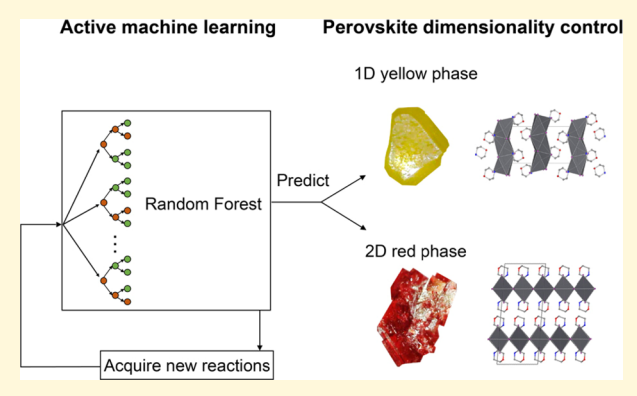
ACCESS

Metrics & More

Article Recommendations

Supporting Information

ABSTRACT: Metal halide perovskite (MHP) derivatives, a promising class of optoelectronic materials, have been synthesized with a range of dimensionalities that govern their optoelectronic properties and determine their applications. We demonstrate a data-driven approach combining active learning and high-throughput experimentation to discover, control, and understand the formation of phases with different dimensionalities in the morpholinium (morph) lead iodide system. Using a robot-assisted workflow, we synthesized and characterized two novel MHP derivatives that have distinct optical properties: a one-dimensional (1D) morphPbI₃ phase ($[C_4H_{10}NO]$ - $[PbI_3]$) and a two-dimensional (2D) (morph)₂PbI₄ phase ($[C_4H_{10}NO]_2[PbI_4]$). To efficiently acquire the data needed to construct a machine learning (ML) model of the reaction conditions where the 1D and 2D phases are formed, data acquisition was guided



by a diverse-mini-batch-sampling active learning algorithm, using prediction confidence as a stopping criterion. Querying the ML model uncovered the reaction parameters that have the most significant effects on dimensionality control. Based on these insights, we discuss possible reaction schemes that may selectively promote the formation of morph-Pb-I phases with different dimensionalities. The data-driven approach presented here, including the use of additives to manipulate dimensionality, will be valuable for controlling the crystallization of a range of materials over large reaction-composition spaces.

1. INTRODUCTION

Metal halide perovskite (MHP) derivatives are emerging optoelectronic materials with tunable physical properties and applications in photovoltaic and ferroelectric devices, light-emitting diodes, and lasers. MHP derivatives have been synthesized with diverse crystal structures, with their metal halide frameworks exhibiting connectivities across one, two, or three dimensions. MHP dimensionality (1D, 2D, and 3D) is a critical material parameter because it governs physical properties such as optical absorption, luminescence wavelength, charge transport, and stability.

One strategy for controlling the dimensionality of MHP derivatives is tuning the inorganic or organoammonium Acations that lie between metal halide $[BX_6]^{4-}$ octahedra in the canonical ABX_3 perovskite unit cell. When A-cations are small, with effective radii of 1.7–2.6 Å (e.g., methylammonium),¹⁷ three-dimensional (3D) MHP derivatives form. In contrast, larger cations (>2.6 Å) often give rise to lower-dimensional MHP derivatives.^{18,19} When the cross-sectional area of the cations is larger than 40 Ų, MHP derivatives almost exclusively exhibit zero-dimensional (0D) or one-dimensional (1D) connectivities rather than two-dimensional (2D), owing to steric hindrance.²⁰ For example, heterocyclic organo-

ammonium cations with six or fewer ring members are able to form 2D MHP derivatives with lead iodide, while seven-member and larger rings rarely form in 2D.^{20–23} Despite this limited ability to predict the dimensionalities of heterocyclic organoammonium lead halides, controlling dimensionalities for MHP derivatives incorporating a wide range of cations is still a major challenge.

One factor that complicates the prediction of MHP dimensionality is that different phases in an A–B–X reaction system (e.g., the 3D FAPbBr₃ and 2D FA₂PbBr₄, ²⁴ where FA = formamidinium) may form under different reaction conditions (FA:Pb ratio), given a reaction of A-cations, metal (B²⁺) cations, and halide anions (X $^-$). Controlling dimensionality is a practical challenge for device applications—mixed phases²⁴ in MHP thin films can lead to low device performance.²⁵ Developing design rules for synthesizing MHPs with control-

Received: October 14, 2021 Revised: December 27, 2021



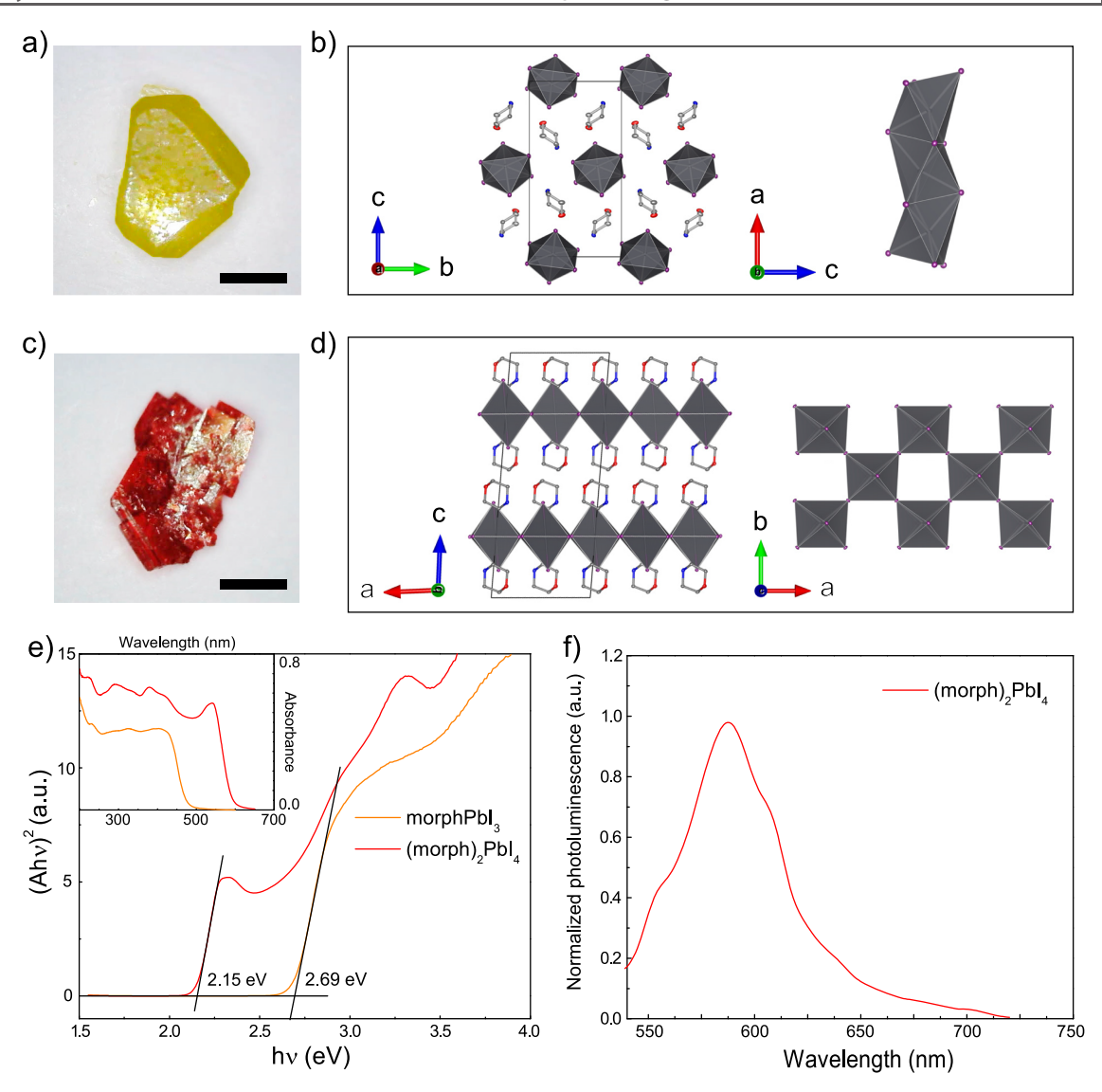


Figure 1. (a) Optical micrograph of a large crystal of the 1D "yellow" phase (scale bar: 1 mm). (b) Packing of $[PbI_{6/2}]^-$ chain structures in morphPbI₃ (1D yellow phase). (c) Optical micrograph of a large crystal of the 2D "red" phase (scale bar: 1 mm). (d) Packing of $[PbI_{2/1}I_{4/2}]^{2-}$ layer structures in (morph)₂PbI₄ (2D red phase). For (b) and (d), dark gray polyhedra represent $[PbI_6]$ octahedra, while purple, light gray, red, and blue atoms correspond to iodine, carbon, oxygen, and nitrogen. Hydrogen atoms have been removed for clarity. (e) Diffuse reflectance spectra of ground powders of morphPbI₃ and (morph)₂PbI₄ in Tauc plots and absorbance units (in the inset). (f) PL spectrum of (morph)₂PbI₄ (λ_{ex} = 470 nm).

lable dimensionalities will drive increases in the performance of real-world MHP devices. Furthermore, understanding the kinetic and thermodynamic factors that influence dimensionality in a single cation-metal-halide (CMH) system will allow us to design functional materials and their reaction pathways. Nevertheless, it is still unclear how to control the dimensionalities of MHP derivatives by tuning the reaction parameters in a single CMH system. Multiple crystalline phases in a single CMH system are typically discovered through trial and error. This time- and resource-intensive approach is particularly inefficient for crystallizing new MHP phases because it can require simultaneous optimization of a large number of experimental variables in high-dimensional experimental parameter space. Insufficient sampling of reaction spaces risks missing rare MHP phases and precludes a comprehensive understanding of the formation of different phases.

Machine learning (ML) and high-throughput experimentation (HTE) have been recently leveraged to accelerate material

discovery and design, 26,27 inspiring our efforts to apply these tools to the crystallization of MHP derivatives.²⁸ However, even with HTE, it can be impractical to perform the large number of experiments needed to train common ML models. To overcome this challenge, researchers have utilized active learning (AL), 29,30 a sequential learning method in which an ML model is iteratively refined over repeated cycles of experimentation through an algorithm that selects new experiments based on the performance of the most recent model. An efficient AL sampling algorithm increases the learning speed of ML models and reduces the number of experiments needed. This efficiency is beneficial for constructing material phase diagrams; 31-33 AL has been used to accelerate the acquisition of phase and composition diagrams of multicomponent materials, including ferroelectric ceramics, ³⁴ piezoelectric materials, ³⁵ phase-change materials, ³⁶ catalysts, ³⁷ and MHP thin films. ³⁸ In these workflows, samples have been typically labeled using data acquired from

simulations, $^{31-33}$ existing datasets, 37 or high-throughput characterization of existing material libraries. $^{36-38}$

Controlling the dimensionality of MHP derivatives requires the analogous task of mapping the reaction conditions that produce specific phases in different regions of synthetic composition space. We hypothesized that an approach combining AL and HTE would be advantageous for building ML models that, given reaction conditions as inputs, predict the phase and dimensionality of MHP products. Solutionphase crystallization of materials presents a stringent test for AL because each reaction tends to be more costly than a simulation or measurement and can involve large numbers of reaction parameters, reagents, and additives. These syntheses are often governed by complex reaction networks³⁹ and stochastic processes (e.g., nucleation) that can lead to noisier and less predictable outcomes than observed with simulation and characterization. These problems are particularly acute when mapping phases across more than three dimensions. When exploring such high-dimensional space, determining when to stop AL experimentation is challenging 40 (and an ongoing subject of research⁴¹) because one cannot determine the actual accuracy of a model without synthesizing a large test set that is representative of the entire experimental space. To realize the potential of AL-guided material synthesis, there is a strong need for robust AL workflows with clear stopping criteria and tolerance for noisy, high-dimensional data.

In this work, we used AL + HTE to discover, control, and understand the formation of MHP derivatives with different dimensionalities in the morpholinium lead iodide (morph-Pb-I) system. We focused on this reaction system because morph⁺ is a six-membered heterocyclic organoammonium that should theoretically form a 2D MHP derivative with PbI₂.²⁰ However, only 1D structures have been observed when morph is combined with different metal cations (e.g., Pb²⁺, Sb⁴⁺) and halides. 42-49 Using HTE, we successfully synthesized the 2D MHP derivative in the morph-Pb-I system. We adopted and modified an AL method to train ML classification models to predict the dimensionalities of phases formed in this chemical system. We established and validated a stopping criterion, based on the model prediction confidence, for terminating experimentation when the ML model was not improving significantly. We used a predictive ML model to uncover the reaction parameters that have the most significant effects on dimensionality control. These insights, combined with density functional theory calculations, allowed us to formulate a plausible reaction scheme that rationalized the formation of MHP derivatives with different dimensionalities in the morph-Pb-I system.

2. RESULTS AND DISCUSSION

2.1. Benchtop Synthesis of Morpholinium Lead lodide. MHP derivative crystals are grown using a range of synthetic methods including seeded crystal growth, ⁵⁰ slow evaporation, ⁵¹ and inverse temperature crystallization. ⁵² In this work, to synthesize morpholinium lead iodide (morph-Pb-I) structures across a range of dimensionalities, we used antisolvent vapor-assisted crystallization (ASVC), a straightforward, room-temperature approach known to produce high-quality MHP crystals suitable for structure determination using single-crystal X-ray diffraction (sXRD). ⁵³ In initial experiments, we manually performed ASVC reactions by exposing a solution of morpholinium iodide and lead iodide (1:1 morph:Pb mole ratio) in dimethylformamide (DMF) to

saturated vapor of dichloromethane (DCM), the antisolvent (scheme illustrated in Figure S1). These benchtop syntheses yielded yellow crystals (Figure 1a). Structural determination based on sXRD confirmed a new MHP derivativemorphPbI3, crystallizing in the orthorhombic space group P2₁2₁2₁ (No. 19). Full crystallographic details of this new phase are given in Table S1; bond length and angles are listed in Tables S2a and S2b, respectively. In morphPbI₃, [PbI₆]⁴⁻ units are arranged in 1D chains of face-sharing octahedra (Figure 1b). The powder XRD (pXRD) pattern of morphPbI₃ matches the pXRD pattern simulated for the sXRD-derived crystal structure (Figure S2a). Tauc analysis of the absorption spectrum of the ground powder of morphPbI3 indicates a direct band gap of 2.69 eV (Figure 1e). No photoluminescence (PL) is detected for this compound. Despite the large band gap and the absence of PL, the 1D yellow phase could have possible applications in second-order nonlinear optics⁵⁴ and piezoelectric devices⁵⁵ owing to its noncentrosymmetric space group (only ~18% of inorganic crystal structures reported are noncentrosymmetric).56

2.2. Robot-Accelerated ASVC Perovskite Workflow. Although we only observed a single 1D morph-Pb-I structure with our isolated benchtop syntheses, 2D derivatives have been predicted theoretically. 20 To more comprehensively search for morph-Pb-I phases of different dimensionalities (especially 2D), we developed a robot-accelerated perovskite workflow based on high-throughput (HT) ASVC to explore a much larger reaction-composition space (see Figure S3 for the workflow). Similar to our previous robot-assisted perovskite investigation and discovery workflow,²⁸ our HT-ASVC workflow utilizes a liquid-handling robot to dispense perovskite precursor solutions into reaction vials. We designed a custom, multiwell ASVC microplate (see Figure \$3; CAD file available⁵⁷) that allowed our liquid-handling robot to prepare 24 parallel ASVC reactions on the 500 μ L scale. Additional details for the HT-ASVC process are described in the Supporting Information. After crystallization, we photographed the reaction vials and recorded the morphologies and colors of the solid products. Then, we characterized the solid products using HT optical microscopy, absorption and PL spectroscopy, and pXRD (HT characterization workflow illustrated in Figure S4). Representative optical micrographs, absorption/PL spectra, and pXRD patterns are shown in Figures S5-S8.

2.3. Primary Screening of 3D Reaction-Composition Space. Using our robotic workflow, we performed primary screening of the reaction-composition space of PbI₂ concentration ([Pb]), morphI concentration ([morph]), and formic acid concentration ([FAH]). We chose this reaction space because our previous HTE work has demonstrated that tuning the analogous concentrations in different ammonium lead halide systems resulted in the successful synthesis of 19 MHP derivatives from 45 A-cation candidates. We used the Kennard-Stone (KS) algorithm sentence of 19 maps and 19 miles and 19 miles primary reactions from grid points generated in the allowed reaction-composition space (concentration constraints shown in Table S4). KS and grid-point generation algorithms are implemented in the ESCALATE software pipeline we developed to manage HT experiments and capture data. 60

Unlike benchtop syntheses, primary HT-ASVC screening produced both yellow solids and red solids with an unknown structure. Structural determination based on sXRD confirmed that the red crystals (Figure 1c) are a new MHP derivative with formula (morph)₂PbI₄ in the monoclinic space group C2/

c (No. 15, see Tables S1, S3a and S3b for details). In this crystal structure, $[PbI_6]^{4-}$ octahedral units are cornerconnected to form 2D layers (Figure 1d). Therefore, we successfully demonstrated the efficacy of the robotic workflow in the discovery of a new 2D phase in the morph-Pb-I system. This 2D phase was not found during our benchtop syntheses nor has it been experimentally reported in the literature. The 2D red phase has optical properties distinct from the 1D yellow phase. The absorption spectrum of the 2D phase indicates a direct band gap of 2.15 eV, which is 0.54 eV lower than that of the 1D phase (Figure 1e). Under 470 nm excitation, the 2D phase exhibits a broad emission peak at 588 nm (Figure 1f), which could be utilized in the application of light-emitting diodes. Unlike the 1D phase, the 2D phase has a centrosymmetric crystal structure.

Visualizing the distribution of reaction outcomes across the [morph]-[Pb]-[FAH] composition space (Figure 2) illus-

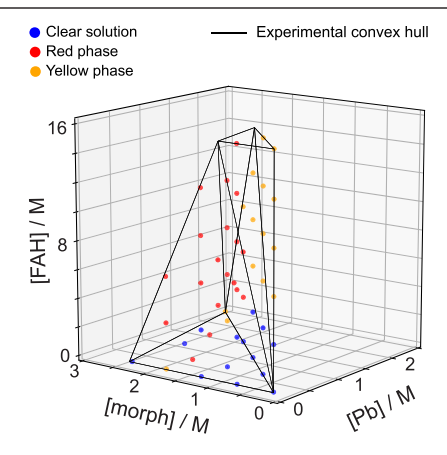


Figure 2. Convex hull of the allowed reaction-composition space (black lines) and the primary screening experiments (colored circles) contained within it, as a function of [Pb], [morph], and [FAH]. The blue circles indicate a clear solution with no crystals. The red and yellow circles indicate reaction outcomes of 2D (red) and 1D (yellow) phases, respectively.

trates how reaction conditions determine the crystallization of the 1D and 2D (red and yellow) phases. For each HT-AVSC experiment in this space, we assigned a reaction outcome from one of the three classes: (1) clear solution, (2) red phase, and (3) yellow phase (see "Product Scoring Rubric Based on Human Inspection" in the Supporting Information). For mixtures of yellow and red products, we labeled the reaction outcomes based on the major product. In general, clear solutions (no solids) were observed below 6 M FAH. Above 6 M FAH, the yellow phase formed at lower morph:Pb ratios (~ 1) , while the red phase was more likely to form at higher morph:Pb. This dependence on the morph-to-Pb ratio is due to the different chemical stoichiometries of the two phases (morph:Pb = 1 in the yellow phase and 2 in the red phase). Tuning the reactant ratio per target-compound stoichiometry has been utilized previously in several CMH systems, such as FA-Pb-Br²⁴. Therefore, not only did primary HT-ASVC screening of the morph-Pb-I system identify a 2D phase, but the resulting dataset also provided guidance for controlling the dimensionality of morph-Pb-I in 3D reaction-composition space.

2.4. Modified Workflow To Screen Additives in Six-Dimensional Reaction-Composition Space. A prevailing

trend in the fabrication of MHP devices is to use mixed solvents and additives to modify the crystallinity and morphology of MHP thin films, which can improve device performance.⁶² However, the effect of these solvents and additives on the dimensionality of MHP products is still unclear. To understand such effects, we simultaneously incorporated four additional solvents and additives into our HT-ASVC reactions. These included three common solvents for MHP syntheses: DMF, dimethyl sulfoxide (DMSO), and γ butyrolactone (GBL). These solvents were selected because of their distinct physical properties, such as their polarity⁶³ and their affinity for coordinating metal ions⁶² and for accepting hydrogen bonds.⁶⁴ We also included water as an additive because our previous study demonstrated that water content in perovskite precursor solutions affects the crystallinity of MHP single crystals and thin films.⁶⁵ Unlike DMSO or DMF, water and formic acid are both hydrogen bond donors and acceptors.⁶⁶ When coexisting in solution, DMSO (or DMF) and water (or formic acid) are likely to form hydrogen bonds. Our new reaction-composition space was thus composed of six reaction parameters: [morph]; [Pb]; the volume fraction of DMSO, $V_{\text{f,DMSO}}$; the volume fraction of GBL, $V_{\text{f,GBL}}$; [FAH]; and the concentration of water, [H₂O]. A seventh parameter, $V_{
m f,DMF}$, was not included in this reaction space because it is calculated as $1 - V_{f,DMSO} - V_{f,GBL}$. The modified roboticsynthesis procedure is described in the Supporting Information, and the constraints of all six parameters are given in Table S5. In the constrained six-dimensional (6D) space, we generated a pool of 469,326 possible reaction compositions located on a fixed grid.

To rapidly characterize the outcomes of reactions performed in this extended 6D space, we acquired absorption spectra on products with a multifunction plate reader. Automated scripts classified reaction products with absorption edges ≥ 2.3 eV as the "yellow phase" and the reactions with absorption edges ≤ 2.15 eV as the "red phase" (see Figure S6a). If no solids formed, we labeled the reaction as a "clear solution." Representative pXRD patterns (Figures S7 and S8) verified that the diffraction peaks of reaction products correspond to the phases predicted using absorption edges.

2.5. Exploring the Role of MHP Additives Using AL. To understand how combinations of additives contribute to the dimensionality of crystals in the morph-Pb-I system, we sought to train an ML model to predict the phase and dimensionality (i.e., 1D yellow phase or 2D red phase) for each combination of reagents in our 6D reaction pool. To train such a model efficiently in such high-dimensional space, we developed an uncertainty-based AL method to perform repeated cycles of HT-ASVC microplate reactions that iteratively refine the ML model. For each cycle in our method, an AL algorithm selects the next batch of reactions to perform by identifying the regions of the 6D reaction-composition space, where the ML model has the highest prediction uncertainty. ^{29,67}

To initiate AL, we performed a uniform sampling of 48 reactions using the KS algorithm. Because visualizing 6D data graphically is difficult, we projected reaction outcomes onto a lower-dimensional space using t-distributed stochastic neighborhood embedding (t-SNE)⁶⁸ (Step 1 in Figure 3). In this initial sampling, we observed all three classes of reaction outcomes. We tested Random Forest (RF) models and Pearson VII universal function kernel-based support-vector

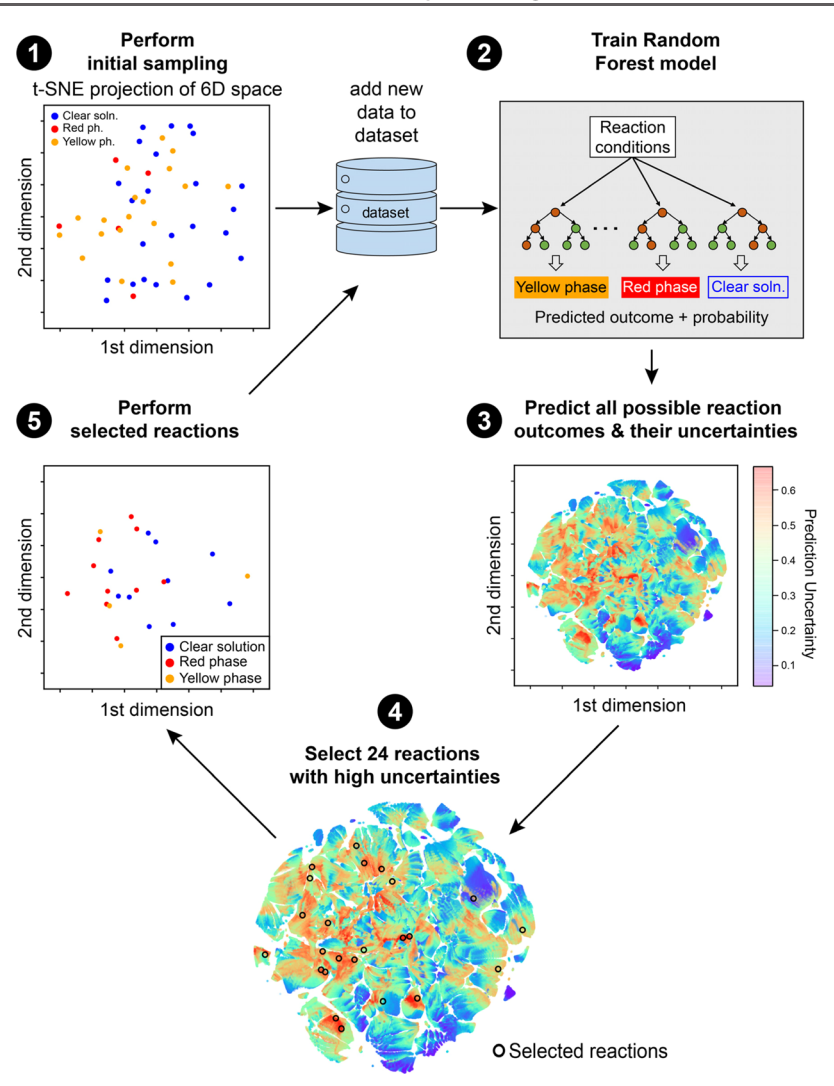


Figure 3. Illustration of the diverse-mini-batch-sampling AL loop. Uniformly sampled seed reactions (Step 1) are used to train an RF model (2), which is then used to calculate prediction uncertainties (3) for the entire pool of potential reactions previously generated in 6D experimental space. In subsequent cycles of AL, reactions are selected using a diverse-mini-batch-sampling algorithm that prioritizes reaction conditions where model predictions have high uncertainty (4). These reactions are performed using a synthesis robot (5), and the data are used to retrain the model and perform additional cycles of active learning (2–5). All AL-sampled reactions (colored scattered circles) and prediction uncertainty distributions (colored maps) are projected onto 2D space using t-distributed stochastic neighborhood embedding (t-SNE).

machine (SVM PUFK) models, optimizing their hyperparameters on the initial dataset using fivefold cross-validation (CV). We selected the RF model as the basis for our AL algorithm because it exhibited the highest CV accuracy of 0.80 \pm 0.09 (Table S6). The RF model, trained by the initial dataset in Step 2, is used to predict reaction outcomes (yellow, red, or no crystals) and calculate the prediction probabilities P for each member of the reaction pool. P is defined as the probability of the reaction outcome predicted to have the highest likelihood of forming (e.g., P = 0.6 if prediction likelihoods are 0.2 for the clear solution, 0.6 for the red phase, and 0.2 for the yellow phase). Then, the prediction uncertainty (U) for each point is calculated as 1 - P (Step 3 in Figure 3). The distribution of U shows that the regions with high uncertainty (U > 0.5) are found where multiple compounds form under similar conditions.

Our AL algorithm is designed to generate the next batch of 24 robot reactions based on the points in reaction-composition space with highest *U.* Simply selecting the 24 reactions with

the highest U, however, would result in reactions with very similar conditions. To avoid such over-sampling in a small region, we implemented the diverse-mini-batch-sampling algorithm, which divides high-uncertainty reactions (U > 0.5) into 24 mini batches using k-mean clustering, weighted by U. Then, the centers of mass of the 24 mini batches are selected as the set of reactions to perform in the next AL cycle. As shown in Step 4 in Figure 3, the selected reactions have diverse reaction conditions and are located in regions of high U. After this batch of reactions is performed and characterized in Step 5, the reaction outcomes are collected and added to the dataset. The updated dataset is then used to retrain the RF model, at which point, the next AL cycle (2-5) commences.

A critical outstanding question in AL-guided materials synthesis is when to terminate the AL loop. In principle, the RF model performance should be evaluated during AL to terminate the AL process when the model ceases to improve, but such evaluation is practically challenging because a large

test set is not available to evaluate the RF model. To determine the stopping point for our AL runs, we monitored the average uncertainty (AU) and prediction confidence (PC) of the RF model after each AL iteration. 71 AU and PC are defined in eqs 1 and 2, respectively:

$$AU = \frac{\sum_{k=1}^{N} U_k}{N} \tag{1}$$

$$PC = \frac{\sum_{k=1}^{N} (P_k - P'_k)}{N}$$
 (2)

Here, N=469,326 is the number of potential reactions in the reaction pool; U_k is the prediction uncertainty for the kth reaction in the reaction pool; P_k and P_k' are the prediction probabilities of the most likely class and second most likely class for the kth reaction. A rising PC (decreasing AU) over AL cycles indicates that AL is still improving the RF model. A decreasing PC (increasing AU) suggests that the RF model has ceased to improve, and AL should be stopped. Heuristically, PC usually increases at the beginning of AL and then decreases, which indicates that ML models were often improved by AL in the first several cycles and then remained little changed. 71,72 In general, adding new data to the training set does not reduce model performance, so decreasing PC implies a lack of improvement rather than a reduction in prediction quality.

After the first AL iteration of 24 reactions, the PC of our RF model increased from 0.41 to 0.45 and AU decreased from 0.34 to 0.32 (Figure 4a), which indicates an improvement of the RF model. Surprisingly, the second AL iteration reduced PC and increased AU, suggesting that experimentation should stop, as the model is no longer improving with the added data points. To confirm the downward trend of PC (and upward trend of AU), we performed three more AL iterations after the

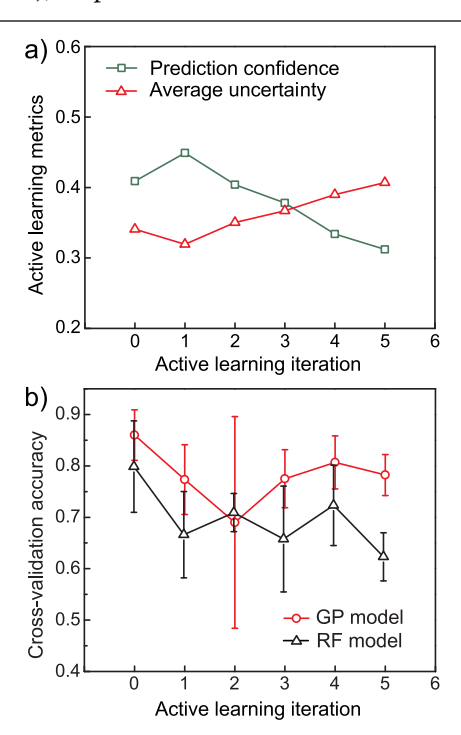


Figure 4. (a) Prediction confidence and average uncertainty of the RF model in each iteration of AL. (b) CV accuracies of the Gaussian process and RF models on the dataset collected after each iteration of AL (error bars represent the standard deviation across fivefold CV).

second iteration. *PC* continued to decrease, so we ceased the AL experiments after the fifth iteration (the practical stopping point). The dataset from AL iterations 2–5 (shown in Figure S9) is included in the training set because expanding a training set rarely reduces the prediction accuracy for the test set.

To justify the practical stopping point, one could, in principle, calculate the prediction accuracy of the RF model (trained by initial sampling +5 AL iterations) over a large test set representative of the overall reaction pool. However, the time and labor required to collect this test set defeat the purpose of AL, which is to minimize the number of experiments. Here, we performed three analyses to support the conclusion that we have reached a reasonable stopping point after five AL iterations.

A good ML model should show modest variance during the last few AL iterations before the practical stopping point (from the second to fifth iteration), 73 shown as small changes in its CV accuracy when including the last few AL runs in the training set. It is worth noting that because the training set has been collected, we are not limited to using RF models in the search for the best ML model. Our first analysis calculated the CV accuracies of multiple ML models after different AL iterations (Table S7 and Figure S10). After the 5th AL iteration, the Gaussian process (GP) model shows the highest CV accuracy of 0.78 ± 0.04 (Figure 4b) and close to the theoretical limit of 0.78 (calculated by overfitting the dataset with deep neural networks, shown in Figure S11).74 The CV accuracy is well above the random-classification (control) accuracy of 0.34 and the majority-class vote accuracy of 0.41. As the most accurate ML model, the GP model shows only a slight variation in the CV accuracy from the second to the fifth AL iteration, which indicates an insignificant variance in the GP model and suggests that the AL experiments have reached the stopping point.

If the most accurate model, the GP model (trained on the dataset after the 5th AL iteration), can accurately predict unseen reaction conditions, AL has likely reached its stopping point. Therefore, in our second analysis, we performed 24 reactions located far from the tested reactions (initial sampling +5 AL runs) in the reaction-composition space (Figure S12a). The 24 reactions were selected using the KS algorithm. The GP model, trained on the tested reactions, shows a prediction accuracy of 0.92 for the unseen 24 reactions (Figure S12b), which leaves little room for improvement and indicates that AL has reached its stopping point.

Testing the AL algorithm on a synthetic dataset (with labels) allows us to monitor the model prediction accuracy for the whole dataset and to investigate whether the stopping criterion based on prediction confidence is reasonable. As the final analysis, we ran the AL algorithm on a synthetic dataset with a similar structure to our experimental dataset (see Figure S13 and the Supporting Information for details). After AL commences, the RF model's PC increases until the fourth AL cycle, after which PC decreases (Figure S14a). Thus, the fourth iteration is considered as the theoretical stopping point. Like our AL experiment, the decreasing trend can be confirmed with a few additional iterations. Meanwhile, the prediction accuracy for the whole dataset rapidly increases from 0.48 (after initial sampling) to 0.82 (after four AL iterations) (Figure S14b). After the 4th cycle, the accuracy plateaus, eventually stabilizing at 0.85 after 100 iterations. Therefore, the model performance has only a 4% improvement with additional 96 AL iterations after the theoretical stopping

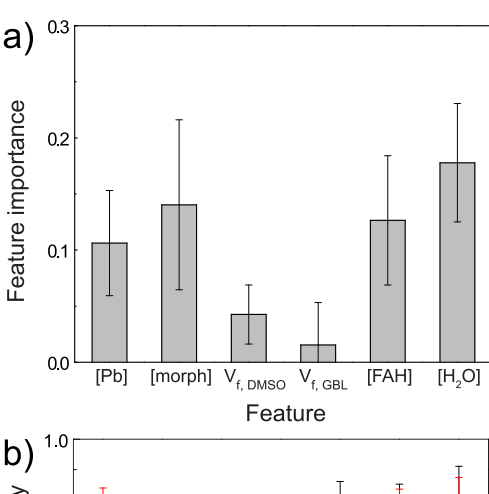
point, confirming that the stopping criterion based on prediction confidence is reasonable. Clear stopping criteria, such as that demonstrated here, will benefit AL-assisted materials and chemistry research.

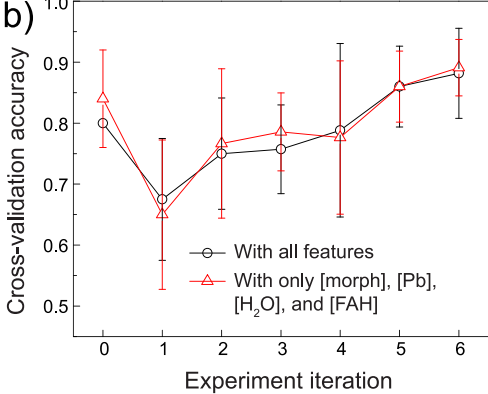
To summarize, we determined the AL stopping point based on the changes in prediction confidence and performed three tractable analyses to support the stopping point. Using diversemini-batch AL and a stopping criterion based on prediction confidence, we only needed to explore at most 0.035% of the reaction pool to successfully build and confirm the stopping point of ML models that accurately predict the formation of the 1D and 2D MHP derivatives in the morph-Pb-I system.

2.6. Importance of Features and Their Effect on **Dimensionality.** A predictive ML model can be used to understand the physicochemical process of morpholinium lead iodide crystallization. To uncover the reaction parameters that have the most significant influence on morph-Pb-I dimensionality, we performed a permutation-feature-importance analysis⁷⁵ (see details in the Supporting Information) on the RF model trained by the portion of the dataset that includes only yellow- and red-phase outcomes. Feature-importance analysis revealed that [Pb], [morph], [FAH], and [H₂O] are important for controlling the formation of 1D and 2D phases (feature importance > 0.1), while the compositions of solvents (i.e., $V_{\rm f,DMSO}$ and $V_{\rm f,GBL}$) are much less important (feature importance < 0.05) and can be ignored (Figure 5a). To validate the feature downselection, we retrained the RF model with the yellow/red dataset and used only [Pb], [morph], [FAH], and [H₂O] as features. Similar CV accuracies were observed compared to the model trained by the full set of features (Figure 5b), suggesting that the feature selection is effective. This analysis is corroborated by the visually distinguishable boundary between yellow and red phases in the parameter space of ln([morph]/[Pb]), [FAH], and $[H_2O]$ (Figure 5c).

To determine whether the important features have positive or negative effects on the formation of the yellow and red phases, we developed a data-driven approach that combines logistic regression (LR) modeling and statistical hypothesis testing. Using a "crystals only" dataset containing only outcomes that produced solids, we performed LR using only [Pb], [morph], [FAH], and [H₂O] as inputs, and with the outcomes labeled as "1" for the yellow phase and "0" for the red phase. Because the LR model demonstrated a reasonable CV accuracy of 0.81 \pm 0.07, the sign of the slope can be treated as the direction of the correlation between the corresponding feature and yellow phase formation. To test the hypotheses with statistical significance, we used bootstrapping⁷⁶ to sample the "crystals only" dataset 1000 times. We fit the 1000 samples into the LR model and obtained a distribution of slopes for each important feature (Figure S16a). The slopes of [morph], [Pb], [FAH], and [H₂O] are $-2.33 \pm$ 0.24, 2.37 ± 0.16 , 1.09 ± 0.24 , and 1.51 ± 0.22 , respectively. Based on this LR analysis, we hypothesized that when solid is formed, [morph] has a negative effect on yellow phase formation while [Pb], [FAH], and [H₂O] have positive effects.

To further validate the correlations between reagent concentrations and crystal phases, we performed one-tailed statistical hypothesis testing. We defined one null hypothesis for each feature: for the yellow phase formation, [morph] is hypothesized to have positive or no effect while [Pb], [FAH], and $[H_2O]$ are hypothesized to have negative or no effect. Given the mean values and standard errors of the slopes, we





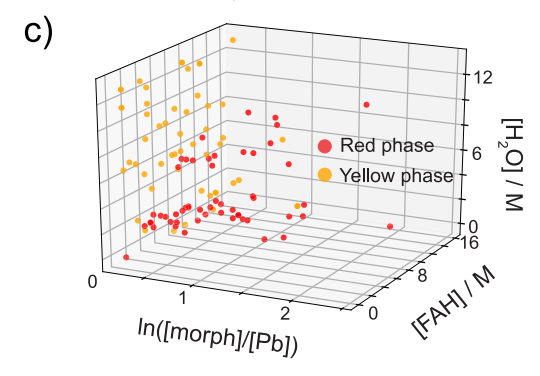


Figure 5. (a) Permutation-feature-importance of the RF model trained by the yellow and red phase reactions. (b) CV accuracies of the RF model on predicting yellow phase vs red phase, with all features (black line) and only [morph], [Pb], $[H_2O]$, and [FAH] (red line). (c) Outcomes of the yellow and red phase reactions as a function of $\ln([morph]/[Pb])$, [FAH], and $[H_2O]$.

rejected all four null hypotheses with a confidence level of 99%. Therefore, all four features have the hypothesized effects on the yellow phase formation. Using the same approach, we discovered that when solid is formed, [morph] has a positive effect on red phase formation while [Pb], [FAH], and $[H_2O]$ have negative effects.

2.7. Understanding the Underlying Physicochemical Process of Dimensionality Control. The effects of [Pb] and [morph] on the dimensionality of morph-Pb-I perovskite derivatives can be largely explained by the chemical stoichiometries of the red and yellow phases. The physicochemical process through which additives (i.e., water and formic acid) influence the dimensionality is still unclear. To understand this physicochemical process, we studied both the thermodynamics and kinetics of the ASVC reaction. First, we investigated whether the reaction is under thermodynamic

control. We calculated the total energy of the yellow phase and red phase using density functional theory (DFT). The DFT calculations show that the yellow phase is slightly more stable than the red phase. However, the formation energy difference between these two phases is negligible ($\Delta E_{\rm form} = 6.8$ kJ per mole of Pb) and within the typical intrinsic error of DFT (~0.1 eV or ~ 10 kJ/mole). Thermogravimetric analysis (TGA) shows that the thermal decomposition temperatures for the yellow and red phases are close (240 and 200 °C, respectively, shown in Figure S17), which agrees with DFT results. DFT calculations also show that only a small amount of energy (33.77 kJ/mol) is needed to convert the yellow phase to the red phase in the solid state (Scheme 1). Theoretically,

Scheme 1. Solid-State Conversion of the Yellow Phase to Red Phase

$$morphPbI_3 + morphI \longrightarrow (morph)_2PbI_4$$

$$\Delta E = 33.77 \text{ kJ} / mol$$

this conversion can be achieved by mechanochemical grinding, which provides an energy of 95–112 kJ/mol.⁸⁰ Ultraviolet—visible (UV—vis) absorption spectra show that at room temperature, the yellow phase can be converted to the red phase in the solid state with one equivalent morphI and manual grinding (Figure 6). The room-temperature synthesis

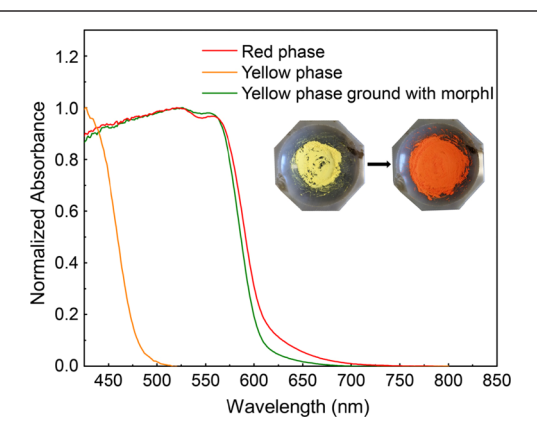
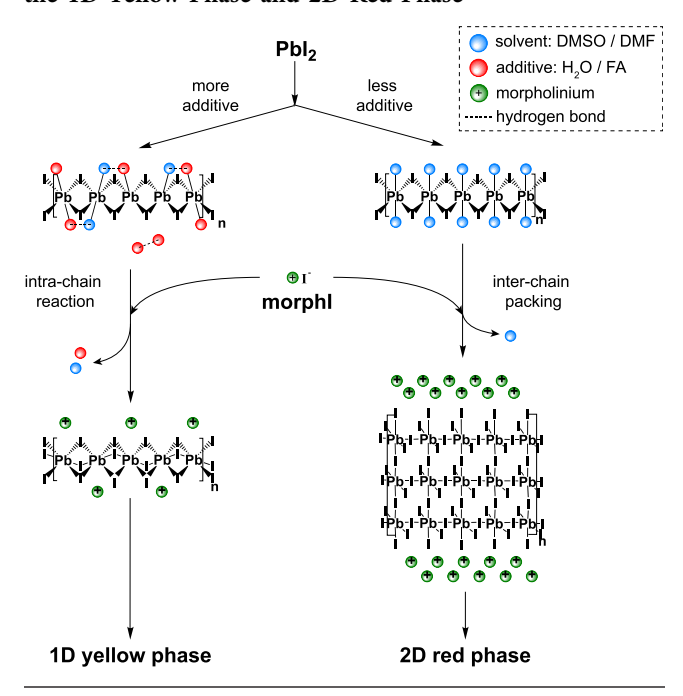


Figure 6. UV—vis absorption spectra of the red phase, yellow phase, and yellow phase ground with additional morphI. The inset photographs are powders of the yellow phase (left) and the yellow phase ground with morphI (right).

of ASVC and the small energy difference between the 1D and 2D phases suggest that the formation of morph-Pb-I phases with varying dimensionalities is not under thermodynamic control.

The small energetic difference between the 1D and 2D phases provides the opportunity for additives such as H₂O and formic acid to exert influence on the dimensionality of the final crystals. LR correlates the use of H₂O and FA with the formation of the 1D yellow phase, but further exploration of the mechanistic origins of such phase selectivity is needed. Experimental and computational investigations of perovskite formation pathways have identified key prenucleation intermediates in the form of 1D chains of PbI₂ coordinated with solvent and additive (e.g., H₂O) molecules. These 1D PbI₂ oligomers, shown in Scheme 2, may be converted into the 1D lead iodide frameworks in yellow-phase morphPbI₃ or may stack into the 2D lead iodide frameworks of the red phase.

Scheme 2. Possible Reaction Scheme for the Formation of the 1D Yellow Phase and 2D Red Phase



Because intramolecular hydrogen bonding in proteins and polymers has been observed to alter their coordination with metal ions,⁸⁴ intrachain H-bonding induced by protic additives may play a role in the phase selectivity imparted by additives in perovskite crystallization. H-bonding between additive and solvent molecules coordinated to adjacent Pb2+ ions on the same 1D PbI₂ chain could geometrically strain metal-ligand bonds (Scheme 2), promoting the dissociation of H-bonded ligand pairs.⁸² Faster dissociation of ligands on neighboring sites could promote the formation of the 1D yellow phase by allowing faster conversion of the 1D prenucleation complexes to the 1D lead iodide frameworks of the morphPbI₃ phase. Meanwhile, slower dissociation could make 1D PbI₂ intermediates more likely to pack with other 1D chains to form the 2D lead iodide framework of the red (morph)₂PbI₄ phase. A more detailed mechanism following this reasoning is provided in Scheme S1 in the Supporting Information. If validated experimentally, the proposed scheme suggests that H₂O and FA additives selectively promote the formation of the 1D morphPbI₃ phase by modulating the reactivity of PbI₃ intermediates via intrachain hydrogen bonding.

3. CONCLUSIONS

Using a robotic workflow based on ASVC, we synthesized two novel MHP derivatives [1D morphPbI₃ and 2D (morph)₂PbI₄] with distinct optical properties. Although the existence (but not crystal structures) of 2D MHP derivatives based on morpholinium has been postulated theoretically, the synthesis and characterization of a 2D derivative has not been reported until this work. We demonstrated the efficacy of the KS sampling algorithm + robotic workflow in finding rare MHP derivatives. Using the uncertainty-based AL method with decreased prediction confidence as a stopping criterion, we sampled only 0.035% of the reaction-composition space to build a predictive ML model to classify the reaction conditions where 1D and 2D phases are formed. By analyzing the feature importance of the predictive ML model, we elucidated that

[Pb], [morph], [FAH], and [H₂O] have significant influence on the dimensionality control in the morph-Pb-I system. Using these data, along with DFT calculations, thermogravimetric measurements, and mechanochemistry observations, we explored the mechanistic origins of the selective formation of the 1D and 2D phases. In one possible scheme, water and formic acid may accelerate the formation of the 1D phase via intrachain hydrogen bonding, which could be observed with other A-cations and MHP systems. Our strategy of using additives to control dimensionality has the potential to be applied in many other CMH systems. With the AL stopping criterion developed and tested in this work, the AL + HTE approach will be valuable for any material research that benefits from predicting and controlling different phases/compounds in a vast reaction-composition space.

4. METHODS

4.1. Materials. Lead iodide (PbI₂) (99%), formic acid (FAH) (\geq 95%), dimethylformamide (DMF) (99.8%), dimethyl sulfoxide (DMSO) (\geq 99.5%), and dichloromethane (DCM) (\geq 99.8%) were purchased from Sigma Aldrich Chemicals. γ -Butyrolactone (GBL) (\geq 98%) was purchased from Spectrum Chemical. Morpholinium iodide (morphI) (98%) was purchased from GreatCell Solar.

4.2. Robotic Workflow. Our HT-ASVC workflow utilizes a Hamilton Microlab NIMBUS4 liquid-handling robot equipped with four independent micropipettors. Stock solutions of PbI2-morphI mixture solution and morphI solution were prepared based on experimental data entry files generated by ESCALATE60 using the solubility data. After stock solution preparation, all reaction components (i.e., the stock solutions, pure solvents, and additives) were placed in programmatically designated locations on NIMBUS operation deck. A synthetic flow chart describing stock solution preparation and robotic procedures is shown in Figure S3 in the Supporting Information. A customized robot-compatible crystallization block, containing 24 pairs of wells, was placed on the Hamilton Heater Shaker module. For one pair of wells in the block, perovskite stock solution occupied one well, and the other well contained the antisolvent (DCM). The 8 × 43 mm (diameter × height) glass scintillation vials were used as reaction and antisolvent vessels. The vials were maintained at 75 °C during the addition of the stock solutions for dissolution. Formic acid was added to each reaction vial, followed by 15 min of shaking to avoid premature precipitation of PbI₂, morphI, or perovskite. After vortexing, the crystallization block was cooled to room temperature before DCM was added to the antisolvent wells in the crystallization block. After DCM addition, we manually sealed the block with a metal cap and stored the block at 20 °C without disturbance for 16 h. Additional details are given in the "Robotic Workflow" section in the Supporting Information.

4.3. Characterization. Powder XRD (pXRD) measurements were performed on a Bruker AXS D8 Discover GADDS X-ray diffractometer with a Vantec-500 area detector and operated at 35 kV/40 mA with a Co K α source with 1.79 Å wavelength. UV-vis absorption spectra were collected using an Agilent Cary-5000 UVvis-near-infrared (NIR) spectrophotometer with an internal diffuse reflectance accessory. PL spectra were measured using a Horiba Jobin Yvon Fluorolog-3 spectrofluorometer and collected from 530 to 720 nm with 1 nm wavelength steps and 0.01 s integration time per step. TGA was performed using TA Instruments Q5500 TGA-MS. The sample weight change was measured from room temperature to 450 °C with a ramp rate of 10 °C/min under nitrogen. HT pXRD measurements were performed on glass slides in a customized sample holder on the same Bruker X-ray diffractometer. The sample locations are programmatically defined in the Bruker GADDS software. HT UV-vis-NIR absorption spectra were collected using a custom-built reflection-mode UV-vis-NIR absorption spectrometer, which has a motorized XY stage to enable automated measurement. The spectra were measured from 350 to 2500 nm and averaged over 100 acquisitions (1 s/acquisition). HT PL spectra were collected using a

Biotek Synergy 4 UV—vis absorption/fluorescence microplate reader. The PL spectra were measured from 540 to 720 nm with 450 nm excitation. HT optical micrographs were acquired using a Biotek Cytation5 Cell Imaging Multimode Reader with a 4× objective lens.

4.4. Reaction Outcome Scoring. All AL reactions from the modified workflow were scored using the UV—vis spectra of the products. The reactions from primary screening were scored by human inspection, with outcomes categorized into three classes: (1) Clear solution: no solid observed in the solutions. (2) Red phase: red crystals or powder are the major solid products. (3) Yellow phase: yellow crystals or powder are the major solid products.

4.5. Software and ML. Our custom-developed pipeline software, ESCALATE, 60 was used to specify experimental parameters in robot readable files, provide instructions for human operators, and capture experiment results and observations. All algorithms in this work were written in Python 3.6 in Jupyter notebooks using the following libraries: Numpy 1.18.0, Pandas 0.22.0, Scipy 1.3.0, Matplotlib 3.1.0, Scikit-learn 0.21.3, and modAL 0.3.5. We used a "Stratified Shuffle Split" method from Scikit-learn to generate training/testing datasets for CV of ML models. In the case of fivefold CV, there are five different train/test splits on the dataset: in each split, 80% of the data were used to train the ML model, while 20% of the data were reserved for testing. The testing sets were randomly drawn from whole datasets in a stratified style (i.e., testing sets have the same percentage of samples of each target class as the whole datasets). Before each drawing, the datasets were shuffled, so the testing datasets are not necessarily exclusive between splits. CV accuracies were calculated by averaging the prediction accuracies of five different train/test splits created by CV on the dataset. Our experimental results were interpreted as either two-class or three-class classification problems. In the two-class case, "yellow phase" outcome was considered as a "positive" result while "red phase" outcome was considered as a "negative" result. The "clear solution" outcomes were excluded. In the three-class case, we calculated the overall prediction accuracy by averaging the prediction accuracies from all possible one-vs-all classifications [e.g., yellow phase (positive) vs nonyellow phase (negative)].

ASSOCIATED CONTENT

Supporting Information

The Supporting Information is available free of charge at https://pubs.acs.org/doi/10.1021/acs.chemmater.1c03564.

Detailed materials and methods; crystal scoring rubric; single crystal structure refinement and CIF files; additional XRD patterns, absorption, and emission spectra; state spaces and metrics for experimental and simulated active learning runs; TGA data; experimental datasets; and Python code used for analysis and experiment generation (PDF)

Crystallographic information for morphPbI₃ (CIF)

Crystallographic information for (morph)₂PbI₄ (CIF)

Python code used for analysis and experiment generation (ZIP)

AUTHOR INFORMATION

Corresponding Author

Emory M. Chan — Molecular Foundry, Lawrence Berkeley National Laboratory, Berkeley, California 94720, United States; orcid.org/0000-0002-5655-0146; Email: EMChan@lbl.gov

Authors

ı

Zhi Li – Molecular Foundry, Lawrence Berkeley National Laboratory, Berkeley, California 94720, United States

- Philip W. Nega Molecular Foundry, Lawrence Berkeley National Laboratory, Berkeley, California 94720, United States
- Mansoor Ani Najeeb Nellikkal Department of Chemistry, Haverford College, Haverford, Pennsylvania 19041, United States; Ocid.org/0000-0002-8258-0613
- Chaochao Dun Molecular Foundry, Lawrence Berkeley National Laboratory, Berkeley, California 94720, United States; orcid.org/0000-0002-3215-6478
- Matthias Zeller Department of Chemistry, Purdue University, West Lafayette, Indianapolis 47907, United States; orcid.org/0000-0002-3305-852X
- Jeffrey J. Urban Molecular Foundry, Lawrence Berkeley National Laboratory, Berkeley, California 94720, United States; orcid.org/0000-0002-6520-830X
- Wissam A. Saidi Department of Mechanical Engineering and Materials Science, University of Pittsburgh, Pittsburgh, Pennsylvania 15261, United States; orcid.org/0000-0001-6714-4832
- Joshua Schrier Department of Chemistry, Fordham University, New York 10458, United States; ⊚ orcid.org/ 0000-0002-2071-1657
- Alexander J. Norquist Department of Chemistry, Haverford College, Haverford, Pennsylvania 19041, United States

Complete contact information is available at: https://pubs.acs.org/10.1021/acs.chemmater.1c03564

Notes

The authors declare no competing financial interest. The CIF files of morphPbI₃ and (morph)₂PbI₄ crystall structures have been submitted to the Cambridge Crystallographic Data Centre under Deposition Numbers 2110021 and 2110022, respectively.

ACKNOWLEDGMENTS

The authors thank Prof. T. Buonassisi and Dr. V. Shekar for helpful discussions. This study is based upon work supported by the Defense Advanced Research Projects Agency (DARPA) under Contract No. HR001118C0036. Any opinions, findings, and conclusions or recommendations expressed in this material are those of the authors and do not necessarily reflect the views of DARPA. Work at the Molecular Foundry was supported by the Office of Science, Office of Basic Energy Sciences, of the U.S. Department of Energy under Contract No. DE-AC02-05CH11231. J.S. acknowledges the Henry Dreyfus Teacher-Scholar Award (TH-14-010) and the resources of the MERCURY consortium (http://mercuryconsortium.org/) under NSF Grant No. CNS-2018427. M.Z. acknowledges the National Science Foundation, Major Research Instrumentation Program under Grant No. CHE 1625543, for funding for the single crystal X-ray diffractometer. W.A.S. acknowledges the support from the U. S. National Science Foundation (Award No. CSSI-2003808). Also, we are grateful for computing time provided in part by the Pittsburgh Center for Research Computing (CRC) resources at the University of Pittsburgh.

REFERENCES

- (1) Herz, L. M. Charge-Carrier Mobilities in Metal Halide Perovskites: Fundamental Mechanisms and Limits. *ACS Energy Lett.* **2017**, *2*, 1539–1548.
- (2) Zhao, Y.; Zhu, K. Organic–Inorganic Hybrid Lead Halide Perovskites for Optoelectronic and Electronic Applications. *Chem. Soc. Rev.* **2016**, *45*, 655–689.

- (3) Takahashi, Y.; Obara, R.; Nakagawa, K.; Nakano, M.; Tokita, J.; Inabe, T. Tunable Charge Transport in Soluble Organic–Inorganic Hybrid Semiconductors. *Chem. Mater.* **2007**, *19*, 6312–6316.
- (4) Leveillee, J.; Katan, C.; Even, J.; Ghosh, D.; Nie, W.; Mohite, A. D.; Tretiak, S.; Schleife, A.; Neukirch, A. J. Tuning Electronic Structure in Layered Hybrid Perovskites with Organic Spacer Substitution. *Nano Lett.* **2019**, *19*, 8732–8740.
- (5) Correa-Baena, J.-P.; Abate, A.; Saliba, M.; Tress, W.; Jacobsson, T. J.; Grätzel, M.; Hagfeldt, A. The Rapid Evolution of Highly Efficient Perovskite Solar Cells. *Energy Environ. Sci.* **2017**, *10*, 710–727.
- (6) Correa-Baena, J.-P.; Saliba, M.; Buonassisi, T.; Grätzel, M.; Abate, A.; Tress, W.; Hagfeldt, A. Promises and Challenges of Perovskite Solar Cells. *Science* **2017**, *358*, 739–744.
- (7) Yang, D.; Luo, L.; Gao, Y.; Chen, S.; Zeng, X. C. Rational Design of One-Dimensional Hybrid Organic—Inorganic Perovskites with Room-Temperature Ferroelectricity and Strong Piezoelectricity. *Mater. Horiz.* **2019**, *6*, 1463—1473.
- (8) Wang, H.-C.; Bao, Z.; Tsai, H.-Y.; Tang, A.-C.; Liu, R.-S. Perovskite Quantum Dots and Their Application in Light-Emitting Diodes. *Small* **2018**, *14*, 1702433–1702455.
- (9) Veldhuis, S. A.; Boix, P. P.; Yantara, N.; Li, M.; Sum, T. C.; Mathews, N.; Mhaisalkar, S. G. Perovskite Materials for Light-Emitting Diodes and Lasers. *Adv. Mater.* **2016**, *28*, *6804*–*6834*.
- (10) Kao, T. S.; Hong, Y.-H.; Hong, K.-B.; Lu, T.-C. Perovskite Random Lasers: A Tunable Coherent Light Source for Emerging Applications. *Nanotechnology* **2021**, *32*, 282001.
- (11) Seth, C.; Jana, D.; Jindal, V.; Khushalani, D.; Ghosh, S. One-Dimensional Behavior of Imidazolium Lead Iodide. *J. Phys. Chem. C* **2019**, *123*, 16449–16455.
- (12) Stoumpos, C. C.; Cao, D. H.; Clark, D. J.; Young, J.; Rondinelli, J. M.; Jang, J. I.; Hupp, J. T.; Kanatzidis, M. G. Ruddlesden—Popper Hybrid Lead Iodide Perovskite 2D Homologous Semiconductors. *Chem. Mater.* **2016**, *28*, 2852–2867.
- (13) Poglitsch, A.; Weber, D. Dynamic Disorder in Methylammoniumtrihalogenoplumbates (II) Observed by Millimeter-wave Spectroscopy. *J. Chem. Phys.* **1987**, *87*, 6373–6378.
- (14) Gao, P.; Bin Mohd Yusoff, A. R.; Nazeeruddin, M. K. Dimensionality Engineering of Hybrid Halide Perovskite Light Absorbers. *Nat. Commun.* **2018**, *9*, 5028.
- (15) Hong, K.; Le, Q. V.; Kim, S. Y.; Jang, H. W. Low-Dimensional Halide Perovskites: Review and Issues. *J. Mater. Chem. C* **2018**, *6*, 2189–2209.
- (16) Yusoff, A. R. B. M.; Nazeeruddin, M. K. Low-Dimensional Perovskites: From Synthesis to Stability in Perovskite Solar Cells. *Adv. Energy Mater.* **2018**, *8*, No. 1702073.
- (17) Kieslich, G.; Sun, S.; Cheetham, A. K. Solid-State Principles Applied to Organic-Inorganic Perovskites: New Tricks for an Old Dog. *Chem. Sci.* **2014**, *5*, 4712–4715.
- (18) Billing, D. G.; Lemmerer, A. Synthesis, Characterization and Phase Transitions in the Inorganic—Organic Layered Perovskite-Type Hybrids [(CnH2n + 1NH3)2PbI4], n = 4, 5 and 6. Acta Crystallogr. B **2007**, 63, 735–747.
- (19) Billing, D. G.; Lemmerer, A. Synthesis, Characterization and Phase Transitions of the Inorganic—Organic Layered Perovskite-Type Hybrids [(CnH2n+1NH3)2PbI4] (n=12, 14, 16 and 18). New J. Chem. **2008**, 32, 1736–1746.
- (20) Saparov, B.; Mitzi, D. B. Organic-Inorganic Perovskites: Structural Versatility for Functional Materials Design. *Chem. Rev.* **2016**, *116*, 4558–4596.
- (21) Billing, D. G.; Lemmerer, A. Inorganic—Organic Hybrid Materials Incorporating Primary Cyclic Ammonium Cations: The Lead Iodide Series. *CrystEngComm* **2007**, *9*, 236–244.
- (22) Billing, D. G.; Lemmerer, A. Inorganic—Organic Hybrid Materials Incorporating Primary Cyclic Ammonium Cations: The Lead Bromide and Chloride Series. *CrystEngComm* **2009**, *11*, 1549—1562.
- (23) Chen, X.-G.; Song, X.-J.; Zhang, Z.-X.; Zhang, H.-Y.; Pan, Q.; Yao, J.; You, Y.-M.; Xiong, R.-G. Confinement-Driven Ferroelectricity

- in a Two-Dimensional Hybrid Lead Iodide Perovskite. J. Am. Chem. Soc. 2020, 142, 10212.
- (24) Fateev, S. A.; Petrov, A. A.; Marchenko, E. I.; Zubavichus, Y. V.; Khrustalev, V. N.; Petrov, A. V.; Aksenov, S. M.; Goodilin, E. A.; Tarasov, A. B. FA2PbBr4: Synthesis, Structure, and Unusual Optical Properties of Two Polymorphs of Formamidinium-Based Layered (110) Hybrid Perovskite. *Chem. Mater.* **2021**, *33*, 1900–1907.
- (25) Huang, J.; Yuan, Y.; Shao, Y.; Yan, Y. Understanding the Physical Properties of Hybrid Perovskites for Photovoltaic Applications. *Nat. Rev. Mater.* **2017**, *2*, 17042.
- (26) Stach, E.; DeCost, B.; Kusne, A. G.; Hattrick-Simpers, J.; Brown, K. A.; Reyes, K. G.; Schrier, J.; Billinge, S.; Buonassisi, T.; Foster, I.; Gomes, C. P.; Gregoire, J. M.; Mehta, A.; Montoya, J.; Olivetti, E.; Park, C.; Rotenberg, E.; Saikin, S. K.; Smullin, S.; Stanev, V.; Maruyama, B. Autonomous Experimentation Systems for Materials Development: A Community Perspective. *Matter* 2021, 4, 2702–2726.
- (27) Liu, Y.; Niu, C.; Wang, Z.; Gan, Y.; Zhu, Y.; Sun, S.; Shen, T. Machine Learning in Materials Genome Initiative: A Review. *J. Mater. Sci. Technol.* **2020**, *57*, 113.
- (28) Li, Z.; Najeeb, M. A.; Alves, L.; Sherman, A. Z.; Shekar, V.; Cruz Parrilla, P.; Pendleton, I. M.; Wang, W.; Nega, P. W.; Zeller, M.; Schrier, J.; Norquist, A. J.; Chan, E. M. Robot-Accelerated Perovskite Investigation and Discovery. *Chem. Mater.* **2020**, *32*, 5650–5663.
- (29) Lookman, T.; Balachandran, P. V.; Xue, D.; Yuan, R. Active Learning in Materials Science with Emphasis on Adaptive Sampling Using Uncertainties for Targeted Design. *npj Comput. Mater.* **2019**, *5*, 1–17.
- (30) del Rosario, Z.; Rupp, M.; Kim, Y.; Antono, E.; Ling, J. Assessing the Frontier: Active Learning, Model Accuracy, and Multi-Objective Candidate Discovery and Optimization. *J. Chem. Phys.* **2020**, *153*, No. 024112.
- (31) Dai, C.; Glotzer, S. C. Efficient Phase Diagram Sampling by Active Learning. *J. Phys. Chem. B* **2020**, *124*, 1275–1284.
- (32) Zhao, S.; Cai, T.; Zhang, L.; Li, W.; Lin, J. Autonomous Construction of Phase Diagrams of Block Copolymers by Theory-Assisted Active Machine Learning. ACS Macro Lett. 2021, 10, 598–602
- (33) Tian, Y.; Yuan, R.; Xue, D.; Zhou, Y.; Wang, Y.; Ding, X.; Sun, J.; Lookman, T. Determining Multi-Component Phase Diagrams with Desired Characteristics Using Active Learning. *Adv. Sci.* **2021**, 8, No. 2003165.
- (34) Balachandran, P. V.; Kowalski, B.; Sehirlioglu, A.; Lookman, T. Experimental Search for High-Temperature Ferroelectric Perovskites Guided by Two-Step Machine Learning. *Nat. Commun.* **2018**, *9*, 1668.
- (35) Xue, D.; Balachandran, P. V.; Yuan, R.; Hu, T.; Qian, X.; Dougherty, E. R.; Lookman, T. Accelerated Search for BaTiO3-Based Piezoelectrics with Vertical Morphotropic Phase Boundary Using Bayesian Learning. *Proc. Natl. Acad. Sci. U.S. A.* **2016**, *113*, 13301–13306.
- (36) Kusne, A. G.; Yu, H.; Wu, C.; Zhang, H.; Hattrick-Simpers, J.; DeCost, B.; Sarker, S.; Oses, C.; Toher, C.; Curtarolo, S.; Davydov, A. V.; Agarwal, R.; Bendersky, L. A.; Li, M.; Mehta, A.; Takeuchi, I. Onthe-Fly Closed-Loop Materials Discovery via Bayesian Active Learning. *Nat. Commun.* 2020, *11*, 5966.
- (37) Rohr, B.; Stein, H. S.; Guevarra, D.; Wang, Y.; Haber, J. A.; Aykol, M.; Suram, S. K.; Gregoire, J. M. Benchmarking the Acceleration of Materials Discovery by Sequential Learning. *Chem. Sci.* **2020**, *11*, 2696–2706.
- (38) Sun, S.; Tiihonen, A.; Oviedo, F.; Liu, Z.; Thapa, J.; Zhao, Y.; Hartono, N. T. P.; Goyal, A.; Heumueller, T.; Batali, C.; Encinas, A.; Yoo, J. J.; Li, R.; Ren, Z.; Peters, I. M.; Brabec, C. J.; Bawendi, M. G.; Stevanovic, V.; Fisher, J.; Buonassisi, T. A Data Fusion Approach to Optimize Compositional Stability of Halide Perovskites. *Matter* **2021**, *4*, 1305–1322.
- (39) Dahl, J. C.; Wang, X.; Huang, X.; Chan, E. M.; Alivisatos, A. P. Elucidating the Weakly Reversible Cs–Pb–Br Perovskite Nanocrystal Reaction Network with High-Throughput Maps and Transformations. *J. Am. Chem. Soc.* **2020**, *142*, 11915–11926.

- (40) Hino, H. Active Learning: Problem Settings and Recent Developments, 2020. arXiv: 2012.04225 (Computer Science and Machine Learning). https://arxiv.org/abs/2012.04225.
- (41) Ueno, T.; Ishibashi, H.; Hino, H.; Ono, K. Automated Stopping Criterion for Spectral Measurements with Active Learning. *npj Comput. Mater.* **2021**, *7*, 1–9.
- (42) Ramalingam, K.; Rajaraman, T. Metal Organic Hybrids of Tin(IV) with Tuneable Band Gap: Synthesis, Spectral, Single Crystal X-Ray Structural, BVS and CSM Analysis of Morpholinium Hexahalostannate(IV). J. Mol. Struct. 2020, 1218, No. 128489.
- (43) Xiong, K.; Liu, W.; Teat, S. J.; An, L.; Wang, H.; Emge, T. J.; Li, J. New Hybrid Lead Iodides: From One-Dimensional Chain to Two-Dimensional Layered Perovskite Structure. *J. Solid State Chem.* **2015**, 230, 143–148.
- (44) Owczarek, M.; Jakubas, R.; Pietraszko, A.; Medycki, W.; Baran, J. Investigation of Structure—Properties Relationship in a Novel Family of Halogenoantimonates(III) and Halogenobismuthates(III) with Morpholinium Cation: [NH2(C2H4)2O]MX4. Crystal Structure, Phase Transitions and Dynamics of Molecules. *Dalton Trans.* **2013**, *42*, 15069—15079.
- (45) Owczarek, M.; Szklarz, P.; Jakubas, R.; Miniewicz, A. [NH2(C2H4)2O]MX5: A New Family of Morpholinium Nonlinear Optical Materials among Halogenoantimonate(III) and Halogenobismuthate(III) Compounds. Structural Characterization, Dielectric and Piezoelectric Properties. *Dalton Trans.* **2012**, 41, 7285–7294.
- (46) Kawasaki, T.; Takahashi, M.; Ohhara, T.; Tanaka, I.; Kusaka, K.; Hosoya, T.; Yamada, T.; Kurihara, K. Structure of Morpholinium Tribromoplumbate C4H8ONH2PbBr3 Studied Using Single-Crystal Neutron Diffraction. *J. Phys. Soc. Jpn.* **2012**, *81*, No. 094602.
- (47) Li, H.-H.; Chen, Z.-R.; Cheng, L.-C.; Wang, Y.-J.; Feng, M.; Wang, M. Hybrid Polymeric Iodoplumbates Constructed from Morpholine and Its Derivatives: Structures and Properties. *Dalton Trans.* **2010**, *39*, 11000–11007.
- (48) Li, H.-H.; Chen, Z.-R.; Cheng, L.-C.; Liu, J.-B.; Chen, X.-B.; Li, J.-Q. A New Hybrid Optical Semiconductor Based on Polymeric Iodoplumbate Co-Templated by Both Organic Cation and Polyiodide Anion. *Cryst. Growth Des.* **2008**, *8*, 4355–4358.
- (49) Corradi, A. B.; Bruni, S.; Cariati, F.; Ferrari, A. M.; Saccani, A.; Sandrolini, F.; Sgarabotto, P. Organic/Inorganic Composite Materials: Synthesis and Properties of One-Dimensional Polymeric Haloplumbate(II) Systems. *Inorg. Chim. Acta* 1997, 254, 137–143.
- (50) Yue, H.-L.; Sung, H.-H.; Chen, F.-C. Seeded Space-Limited Crystallization of CH3NH3PbI3 Single-Crystal Plates for Perovskite Solar Cells. *Adv. Electron. Mater.* **2018**, *4*, No. 1700655.
- (51) Shi, C.; Ye, L.; Gong, Z.-X.; Ma, J.-J.; Wang, Q.-W.; Jiang, J.-Y.; Hua, M.-M.; Wang, C.-F.; Yu, H.; Zhang, Y.; Ye, H.-Y. Two-Dimensional Organic—Inorganic Hybrid Rare-Earth Double Perovskite Ferroelectrics. *J. Am. Chem. Soc.* **2019**, *142*, 545–551.
- (52) Saidaminov, M. I.; Abdelhady, A. L.; Murali, B.; Alarousu, E.; Burlakov, V. M.; Peng, W.; Dursun, I.; Wang, L.; He, Y.; Maculan, G.; Goriely, A.; Wu, T.; Mohammed, O. F.; Bakr, O. M. High-Quality Bulk Hybrid Perovskite Single Crystals within Minutes by Inverse Temperature Crystallization. *Nat. Commun.* **2015**, *6*, 7586–7592.
- (53) Shi, D.; Adinolfi, V.; Comin, R.; Yuan, M.; Alarousu, E.; Buin, A.; Chen, Y.; Hoogland, S.; Rothenberger, A.; Katsiev, K.; Losovyj, Y.; Zhang, X.; Dowben, P. A.; Mohammed, O. F.; Sargent, E. H.; Bakr, O. M. Low Trap-State Density and Long Carrier Diffusion in Organolead Trihalide Perovskite Single Crystals. *Science* 2015, 347, 519–522.
- (54) Ferrando, A.; Martínez Pastor, J. P.; Suárez, I. Toward Metal Halide Perovskite Nonlinear Photonics. *J. Phys. Chem. Lett.* **2018**, *9*, 5612–5623.
- (55) Park, H.; Ha, C.; Lee, J.-H. Advances in Piezoelectric Halide Perovskites for Energy Harvesting Applications. *J. Mater. Chem. A* **2020**, *8*, 24353–24367.
- (56) Newnham, R. Properties of Materials: Anisotropy, Symmetry, Structure; Oxford University Press: New York, 2005.
- (57) Li, Z. multi-well crystallization block by ZhiLBNL. https://www.thingiverse.com/thing:4927375 (accessed September 20, 2021).

- (58) Kennard, R. W.; Stone, L. A. Computer Aided Design of Experiments. *Technometrics* **1969**, *11*, 137–148.
- (59) Xie, J. Karoka/Kennard-Stone-Algorithm. https://github.com/karoka/Kennard-Stone-Algorithm (accessed September 20, 2021).
- (60) Pendleton, I. M.; Cattabriga, G.; Li, Z.; Najeeb, M. A.; Friedler, S. A.; Norquist, A. J.; Chan, E. M.; Schrier, J. Experiment Specification, Capture and Laboratory Automation Technology (ESCALATE): A Software Pipeline for Automated Chemical Experimentation and Data Management. MRS Commun. 2019, 9, 846–859.
- (61) Yangui, A.; Garrot, D.; Lauret, J. S.; Lusson, A.; Bouchez, G.; Deleporte, E.; Pillet, S.; Bendeif, E. E.; Castro, M.; Triki, S.; Abid, Y.; Boukheddaden, K. Optical Investigation of Broadband White-Light Emission in Self-Assembled Organic—Inorganic Perovskite (C6H11NH3)2PbBr4. J. Phys. Chem. C 2015, 119, 23638–23647.
- (62) Zhou, Y.; Game, O. S.; Pang, S.; Padture, N. P. Microstructures of Organometal Trihalide Perovskites for Solar Cells: Their Evolution from Solutions and Characterization. *J. Phys. Chem. Lett.* **2015**, *6*, 4827–4839.
- (63) Gu, E.; Tang, X.; Langner, S.; Duchstein, P.; Zhao, Y.; Levchuk, I.; Kalancha, V.; Stubhan, T.; Hauch, J.; Egelhaaf, H. J.; Zahn, D.; Osvet, A.; Brabec, C. J. Robot-Based High-Throughput Screening of Antisolvents for Lead Halide Perovskites. *Joule* **2020**, *4*, 1806–1822.
- (64) Islam, T.; Sarker, M. Z. I.; Uddin, A. H.; Yunus, K. B.; Reddy Prasad, D. M.; Mia, M. A. R.; Ferdosh, S. Kamlet Taft Parameters: A Tool to Alternate the Usage of Hazardous Solvent in Pharmaceutical and Chemical Manufacturing/Synthesis A Gateway towards Green Technology. *Anal. Chem. Lett.* 2020, 10, 550–561.
- (65) Nega, P. W.; Li, Z.; Ghosh, V.; Thapa, J.; Sun, S.; Hartono, N. T. P.; Nellikkal, M. A. N.; Norquist, A. J.; Buonassisi, T.; Chan, E. M.; Schrier, J. Using Automated Serendipity to Discover How Trace Water Promotes and Inhibits Lead Halide Perovskite Crystal Formation. *Appl. Phys. Lett.* **2021**, *119*, No. 041903.
- (66) Kamlet-Taft solvent parameters. http://www.stenutz.eu/chem/solv26.php (accessed May 17, 2021).
- (67) Settles, B. Active Learning Literature Survey. University of Wisconsin-Madison, 2010, Vol. 67.
- (68) Hinton, G.; Roweis, S. Stochastic Neighbor Embedding. NIPS'02: Proceedings of the 15th International Conference on Neural Information Processing Systems; MIT Press: Cambridge, MA, United States, 2002; pp 857–864.
- (69) Zhdanov, F. Diverse Mini-Batch Active Learning, 2019. arXiv: 1901.05954 (Computer Science and Machine Learning). https://arxiv.org/abs/1901.05954.
- (70) MacQueen, J. Some Methods for Classification and Analysis of Multivariate Observations. *Proceedings of the Fifth Berkeley Symposium on Mathematical Statistics and Probability, Volume 1: Statistics*; University of California Press, 1967; pp 281–297.
- (71) Vlachos, A. A Stopping Criterion for Active Learning. Comput. Speech Lang. 2008, 22, 295–312.
- (72) Zhu, J.; Wang, H.; Hovy, E.; Ma, M. Confidence-Based Stopping Criteria for Active Learning for Data Annotation. *ACM Trans. Speech Lang. Process.* **2010**, *6*, 1–24.
- (73) Yang, Y.; Loog, M. A Variance Maximization Criterion for Active Learning. *Pattern Recognit.* **2018**, 78, 358–370.
- (74) Cortes, C.; Jackel, L. D.; Chiang, W.-P. Limits on Learning Machine Accuracy Imposed by Data Quality. KDD'95: Proceedings of the First International Conference on Knowledge Discovery and Data Mining; AAAI Press, 1995; pp 57–62.
- (75) 4.2. Permutation feature importance scikit-learn 0.24.2 documentation. https://scikit-learn.org/stable/modules/permutation_importance.html#outline-of-the-permutation-importance-algorithm (accessed June 3, 2021).
- (76) Efron, B.; Tibshirani, R. Bootstrap Methods for Standard Errors, Confidence Intervals, and Other Measures of Statistical Accuracy. *Stat. Sci.* **1986**, *1*, 54–75.
- (77) Lehmann, E. L.; Romano, J. P. *Testing Statistical Hypotheses*, 3rd ed.; Springer Texts in Statistics; Springer-Verlag: New York, 2005, DOI: 10.1007/0-387-27605-X.

- (78) Perdew, J. P.; Ruzsinszky, A.; Csonka, G. I.; Vydrov, O. A.; Scuseria, G. E.; Constantin, L. A.; Zhou, X.; Burke, K. Restoring the Density-Gradient Expansion for Exchange in Solids and Surfaces. *Phys. Rev. Lett.* **2008**, *100*, No. 136406.
- (79) Kirklin, S.; Saal, J. E.; Meredig, B.; Thompson, A.; Doak, J. W.; Aykol, M.; Rühl, S.; Wolverton, C. The Open Quantum Materials Database (OQMD): Assessing the Accuracy of DFT Formation Energies. *npj Comput. Mater.* **2015**, *1*, 1–15.
- (80) Do, J.-L.; Friščić, T. Mechanochemistry: A Force of Synthesis. ACS Cent. Sci. 2017, 3, 13–19.
- (81) Guo, Y.; Shoyama, K.; Sato, W.; Matsuo, Y.; Inoue, K.; Harano, K.; Liu, C.; Tanaka, H.; Nakamura, E. Chemical Pathways Connecting Lead(II) Iodide and Perovskite via Polymeric Plumbate(II) Fiber. J. Am. Chem. Soc. 2015, 137, 15907—15914.
- (82) Zhang, K.; Wang, Z.; Wang, G.; Wang, J.; Li, Y.; Qian, W.; Zheng, S.; Xiao, S.; Yang, S. A Prenucleation Strategy for Ambient Fabrication of Perovskite Solar Cells with High Device Performance Uniformity. *Nat. Commun.* **2020**, *11*, 1006.
- (83) Xiao, S.; Zhang, K.; Zheng, S.; Yang, S. Good or Evil: What Is the Role of Water in Crystallization of Organometal Halide Perovskites? *Nanoscale Horiz.* **2020**, *5*, 1147–1154.
- (84) Natale, D.; Mareque-Rivas, J. C. The Combination of Transition Metal Ions and Hydrogen-Bonding Interactions. *Chem. Commun.* **2008**, *4*, 425–437.

